Direct-current output of silicon–organic monolayer–platinum Schottky TENGs: Elusive friction-output relationship

Xin Lyu [a], Melanie MacGregor [b], Jun Liu [c], Nadim Darwish [a], Simone Ciampi [a,*]

[a] School of Molecular and Life Sciences, Curtin University, Bentley, Western Australia 6102, Australia
[b] Flinders Institute for Nanoscale Science and Technology, Flinders University, Bedford Park, South Australia 5042, Australia
[c] Department of Mechanical and Aerospace Engineering and Research and Education in Energy, Environment and Water Institute, University at Buffalo, The State University of New York, Buffalo, NY 14260, USA

ABSTRACT

Triboelectric nanogenerators (TENGs) are an emerging energy harvesting technology able to convert ubiquitous mechanical energy into electricity. Friction, static charging and flexoelectricity are all involved in the mechanism underpinning TENG operation, but their relative contribution has remained elusive. Here we used dynamic and static conductive atomic force microscopy (C-AFM) measurements on monolayer-modified silicon crystals to detect evidence of a relationship between friction and zero-bias current, and between pressure and the direction of the putative flexovoltage. We demonstrate that a static electricity-related tribovoltage is probably responsible for a friction excess, and that surprisingly this friction excess is found to be dependent on the doping level and type of the silicon substrate. Such friction excess is however no longer measurable once current is allowed to flow across the junction. This observation points to an electrostatic origin of friction in silicon-based Schottky TENGs, and suggests that the zero external bias DC current is at least in part an electronic flow to neutralize static charges. Further, the sign of the zero-bias current, but not its magnitude, is independent of the semiconductor doping type, which is again suggestive of surface statics being a main contributor to the zero-bias output rather than exclusively a space-charge effect. We also reveal the presence of a junction flexovoltage under pressures common in AFM experiments (GPa), even for negligible lateral friction. In a static Pt–monolayer–n-type Si junction the flexovoltage carries the same sign as the tribovoltage, and can reach such magnitude to overwrite external voltages as high as 2 V. The immediate implication is that the flexovoltage is likely to have i) a strong contribution to the zero-bias output of a n-Si Schottky TENG, ii) a negative effect on the output of a p-Si TENG, and iii) its detection can be straightforward, as we discovered that flexoelectricity manifests as an "inverted diode": a n-type Si–platinum diode with negligible current even when the n-type material is negatively biased as long as the "static" diode remains under a large normal pressure.

1. Introduction

The continuous shift from analogue to digital technologies – the so-called digital revolution that started around 1980 – has transformed society [1,2]. Electronic components at the core of digital devices such as ubiquitous mobile phones, lifesaving pacemakers, niche wearable electronics or microscopic sensors, share a common feature: their operation requires a reliable source of direct current (DC). In most cases, chemical energy stored in a battery remains the source of this DC power. However, all batteries need replacement or periodic recharging, posing a challenge for the continuous operation of devices that are installed in locations of difficult access, such as remote environmental sensors or life-critical medical implants [3–8]. Triboelectric nanogenerators (TENGs) are a class of power sources that convert small-scale vibrations, pressure and mechanical friction into electricity [9–12]. Most TENGs described in the literature are alternated-current TENGs [11,13–15], but over the last five years there has been a substantial increase in the research effort towards the development of DC-TENGs, TENGs outputting DC current and voltage [6,16–28]. Sliding Schottky diodes, that is, out of equilibrium metal–semiconductor junctions under some form of mechanical stress, are a promising form of DC-TENG [17,19,24,26, 29–31], outputting DC densities as high as $\sim 10^9$ A/m^2 for nanoscale contacts, and up to ~ 210 A/m^2 for microscale contacts [24,27]. A complete and correct understanding of the mechanism by which

friction, adhesion and pressure/strain lead to a DC output in a sliding diode is still lacking, but what is clear is that surface engineering by monolayer chemistry is one of the routes towards a better understanding of TENGs' working principles, as well as towards maximizing their output [30,32–34]. For example, the relationship between friction and current output remains unclear [25,35–37]. The zero-bias current output of a Schottky TENG defines its performance as an autonomous power source, and a tribovoltaic effect in response to friction is commonly accepted as the principal mechanism [38–40] leading to such current [36,41]. However, what is also known is that the voltage applied to a rectifying contact, especially in the forward bias, will cause excess friction between metal and semiconductor [37,42]. Surprisingly the origin of this forward-bias-triggered increase in resistance to a lateral movement has not yet been fully explained. The caveat in the TENG context is, of course, that frictional wear will negatively affect the device lifetime [43,44], and should therefore, when possible, be minimized. Friction has been previously reported to influence the triboelectric process [35,45,46], and the influence of electronic drag on friction has also been researched [37,42,44,47], but analogous research on zero-bias rectifying junction is lacking.

Herein we systematically explore the relationship between current output and friction in sliding metal contact–monolayer–semiconductor systems by means of comparing friction and zero-bias current data obtained by atomic force microscopy (AFM) experiments performed with either non-conductive or conductive AFM tips. Changes to the AFM tip but not to the surface chemistry (organic monolayer) of the semiconductor are intended to block, or to allow for, the flow of tribocurrent. This experimental system allows to address open questions such as (i) whether the zero-bias current is purely caused by friction, or whether some of the excess friction is a response to the passage of current and/or generation of a tribovoltage, (ii) whether or not the length of organic monolayer molecular chain (length of the tunnelling barrier) influences the current output [34], and (iii) what is the role and direction of a putative flexovoltage.

The monolayer system we selected to answer the above questions is shown in Scheme 1. A hydrogen-terminated oxide-free silicon surface was covalently derivatized with an organic film by wet chemistry methods [48–54]. Analogous methods of surface passivation and functionalization have been proven effective in improving the performances of TENGs [33,34,55–57], but are underexplored and carry the advantage of a very simple means of tuning at will substrate properties (doping level and type), nature of the top contact (conductive versus insulating), and thickness of the tunneling barrier (monolayer length), all while leaving the outmost surface chemistry of the semiconductor side of the diode unchanged.

2. Results and discussion

Silicon samples used here were stripped of the native oxide layer and then modified with a silicon–carbon-bound hydroxyl-terminated monolayer, as this chemistry introduces an effective surface protection against substrate oxidation (Fig. S1-S2, Supporting Information) and simultaneously yields high triboelectric DC current outputs when used as the semiconductor component of a sliding Schottky diode TENG [27]. The modification of hydrogen-terminated (Si–H) Si(111) with 8-nonyn-1-ol (S1, Scheme 1) has been reported before [27], and an analogous chemical approach with a shorter alkyl chain (4-pentyn-1-ol, 2, Scheme 1) was also successful in yielding an oxide-free surface (S2, Figs. S3-S4, Supporting Information).

### 2.1. Relationship between zero-bias current and friction

It is commonly accepted that in a Schottky TENG friction induces a current flow by generating electron–hole pairs [36]. Equally accepted is that current output is proportional to friction [41,58–62]. An effective way to improve the current output therefore could be to increase friction by establishing closer contact through increasing the applied load [63]. Unfortunately such gain will come undoubtedly at the cost of reducing the lifespan of the triboelectric material [43,64]. Hence, a detailed exploration on the relationship between current and friction is necessary, especially to understand the cause–effect relationship questioned in the introduction section.

In an AFM experiment friction and current signals can be recorded simultaneously. Given the possibility of an electronic contribution to friction [37,42] we carried out a simple but very informative experiment with an insulating top contact (Si AFM tip) such to block the flow of DC current. The choice of a non- conductive top contact removes the possibility of an electronic drag force but obviously leaves the possibility of an electrostatics build-up and consequent attractive forces.

Fig. 1 shows topography and current AFM maps for 8-nonyn-1-ol coated Si(111) substrates (S1) of different doping type and level, acquired with either conductive platinum or non-conductive silicon tips.
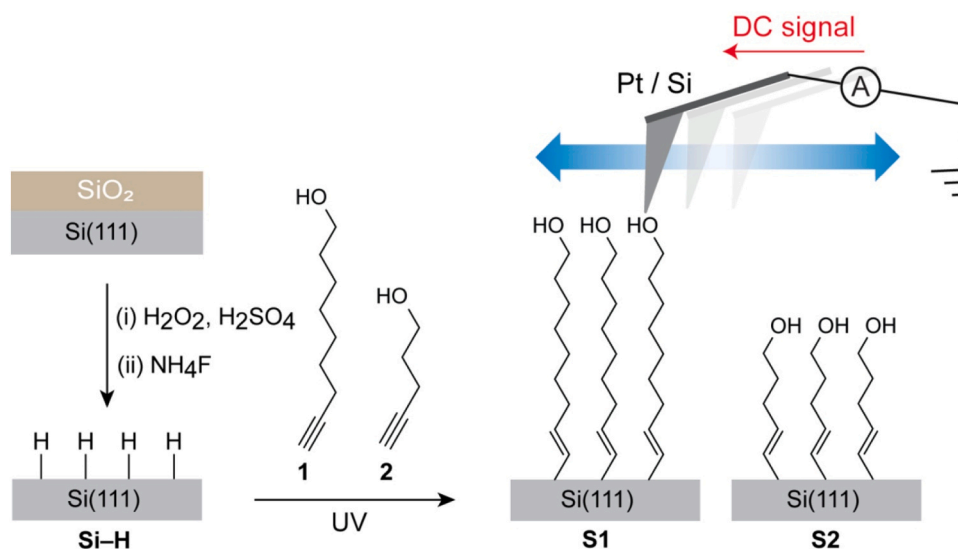
Scheme 1. Surface passivation and functionalization of oxide-free Si(111) substrates. Silicon surfaces were (i) cleaned with Piranha solution and (ii) etched in ammonium fluoride aqueous solutions. The hydrogen-terminated samples (Si–H) were then reacted with either 8-nonyn-1-ol (1), or 4-pentyn-1-ol (2) under UV light to yield the monolayer-modified Si(111) surfaces S1 and S2, respectively.
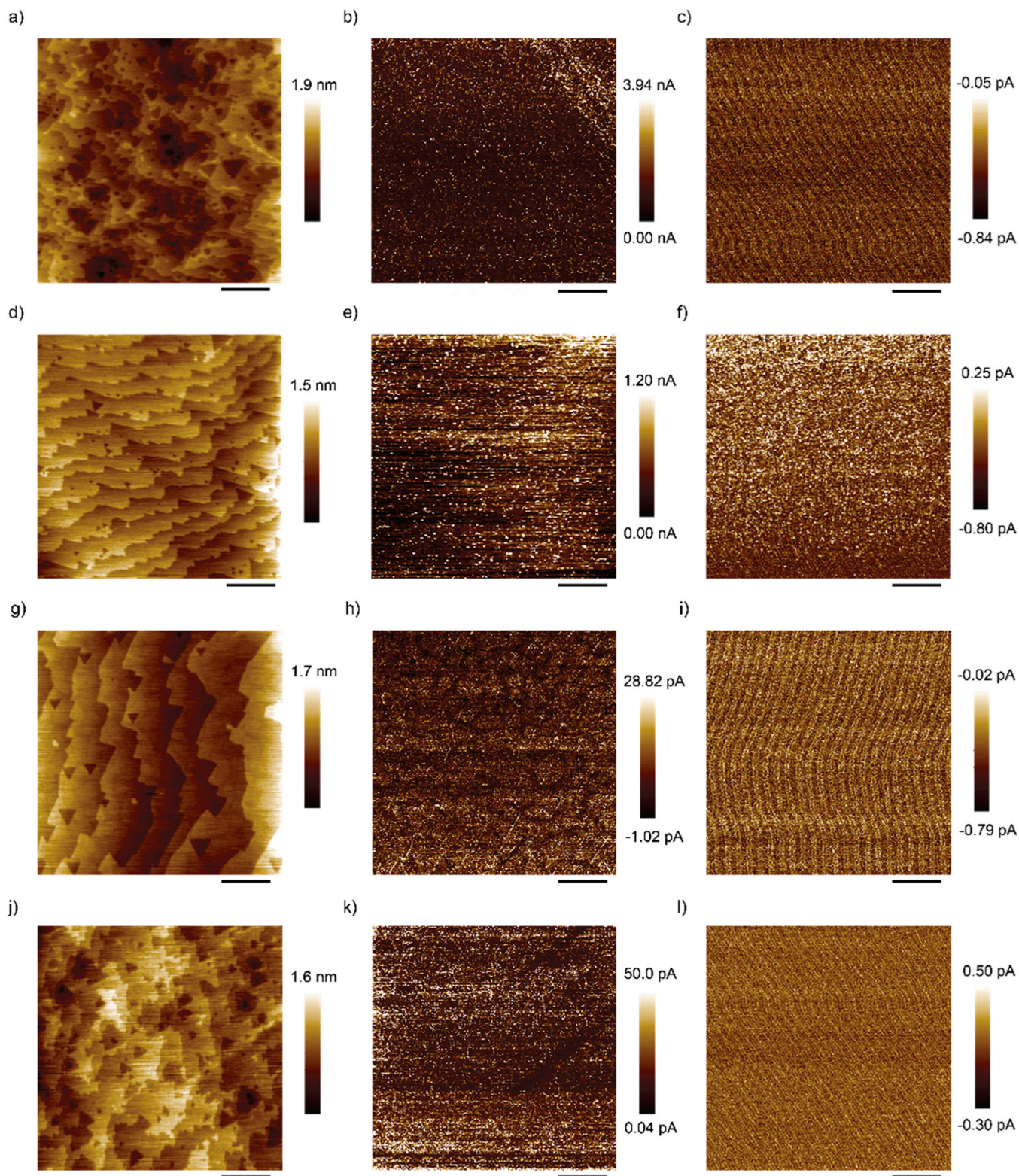
Fig. 1. AFM height 5 × 5 μm images of 8-nonyn-1-ol coated (**S1**) samples prepared on either lowly doped n-type (a), highly doped n-type (d), lowly doped p-type (g), or highly doped p-type (j) Si(111) substrates, and the corresponding zero-bias current C-AFM maps recorded with either conductive platinum tips (b, e, h, k) or non-conductive silicon tips (c, f, i, l). The scale bars in all panels represent 1 μm. The applied force was set to 360 nN.

Using sliding platinum AFM tips, the highest zero-bias DC signal was recorded on lowly doped n-type **S1** Si(111) substrates (Fig. 1b). This doping level and type had the highest output among all the different doping levels tested (Fig. 1b,e,h,k), with the maximum current density reaching up to $4.40 \pm 0.85 \times 10^7$ A/m^2. The current density recorded on highly-doped n-type Si(111) substrates comes as second high, with a value of $1.60 \pm 0.40 \times 10^7$ A/m^2, followed by highly-doped p-type Si (111) with $6.45 \pm 0.31 \times 10^5$ A/m^2, and then by lowly-doped p-type Si (111) substrates, $3.25 \pm 0.79 \times 10^5$ A/m^2. As evident from the data in Fig. 1, the experimental zero-bias currents are of positive sign on all

samples, indicating a flow of electrons from tip to sample. This is the direction of a leakage current in a n-type Si–Pt junction, but of a forward current on a p-type based junction. To further probe the relationship between doping level and zero-bias current we also performed measurements on samples of intermediate doping (Fig. S5, Supporting Information). The maximum current density reached up to $1.73 \pm 0.43 \times 10^7$ A/m^2, which is intermediate between the lowly doped and highly doped silicon substrates. We also note that higher current outputs tend to be localized at the edge of the Si(111) terraces, which are likely to expose more conductive Si(211) planes [27]. As shown in Fig. 1c,f,i,l, current mapping of samples analyzed with non-conductive tips exhibited, as expected, only electrical noise.

To qualitatively determine the samples' friction coefficients, the normalized mean experimental friction was plotted against the applied load (Fig. 2). When using conductive tips, the friction coefficients (represented by the slope of the regression lines in Fig. 2) of junctions made on all four substrates (**S1** samples on lowly doped n-type, highly doped n-type, lowly doped p-type, and highly doped p-type) are quite similar, and the actual friction values were all of relatively low level compared to those recorded with non-conductive AFM tips. Remarkably, for the same surface chemistry, when the flow of DC current was deliberately blocked by using non-conductive tips, the friction data across the four doping types and levels varied significantly. The changes in friction observed across the four samples using non-conductive tips tracked closely the magnitude of the zero-bias current recorded with conductive tips shown in Fig. 1b,e,h,k. The higher the sample's zero-bias current (conductive tips), the more friction was observed under open-circuit conditions (insulating tips). The current data are the first reported evidence of a difference in friction, under no external bias [37], linked to changes to the doping type and level of silicon, and although this difference can be tentatively ascribed to differences in surface statics, a direct evidence is unfortunately lacking. To the best of our knowledge there are no experimental evidence pointing to different propensity for silicon to gain surface static charges based on differences in bulk doping type and level – doped silicon position in the triboelectric series is unclear [65]. For some semiconductors there is an established link between the material work function and its position in the triboelectric series, but similar data are not available for silicon, and any attempt to measure the static charging of a macroscopic silicon sample with a Faraday pail lead to charge readings below the detection limit of our setup (~0.1 nC/cm^2). Based on the parallel between Fig. 1 and Fig. 2 (high friction at open circuit and TENG current) we propose that tribocurrents recorded with Pt tips are at least in part a flow of current such

to neutralize static charging of the junction, and conversely that increase in friction, when the current cannot flow because of the insulating character of the tip, is a lateral tilt of the tip caused by statics.

To further prove this last point we recorded force–distance (F–D) curves on lowly-doped n-type Si(111) surfaces coated with 8-nonyn-1-ol by (**S1**) under UV light (250 −260 nm), so to use the UV-mediated ionization of air to gradually eliminate surface static charges [66,67]. Fig. S6 (Supporting Information) shows the adhesion force between the lowly doped **S1** sample and a non-conductive tip. All the reported adhesion forces are the mean value of 100 measurements at spots evenly distributed across the imaging region shown in Fig. 1a. UV light was initially kept off, and a first set of F–D measurements (1st test) performed, which returned a surface adhesion force of 436.88 ± 14.52 nN. The UV light was then switched on for 20 s, causing surface adhesion to drop significantly (364.83 ± 8.84 nN, 2nd test). The adhesion force kept decreasing with increasing UV exposure times (2nd to 6th test). After six 20-s cycles of UV illumination the surface adhesion force reached a plateau of 306.36 ± 5.21 nN. Finally, to further verify that the sliding diode motion causes statics we conducted F–D measurements again after another whole region scan (8th test). The adhesion force returned back to 370.77 ± 18.58 nN, which is ~6 nN higher than the 2nd test results (1st UV cycle). These results indicate that surface statics is established upon tip sliding over the sample, but these charges are nearly completely (but not entirely) neutralized by ionized species formed upon UV illumination. Electrostatic charging, which at least in his sign appears to be independent of the silicon doping level and type, is therefore a clear contributor to the DC tribocurrent measured with Pt tips, although, as stated above, when measured with Pt tips, any sizable difference in friction between samples disappears.

Another interesting finding from the above section is that regardless of the silicon substrate doping type, the zero-bias current (Fig. 1b,e,h,k) have the same direction: from semiconductor to metal. One reason could be Fermi level pinning caused by the introduction of the large number of surface states on the 8-nonyn-1-ol coated Si surfaces [27,68]. Contributing to these surface states could be deprotonation of the monolayer terminal functional group (R–OH) to alkoxide anion (R–O$^-$) [69–71]. Another reason for the sign of the tribocurrent not varying with the doping type of the substrate could be that a flexoelectric band bending and ratcheting mechanism [72] are present and lead to a flexovoltage independent of doping type.

2.2. Carbon chain length and tribocurrent

Following from the conclusion of the previous section, we then tried to answer the question on the role of surface alkoxide anions, which in part resembles a question first raised by Wang and co-workers in 2016 [34], that is whether or not the length a molecular carbon chain influences the zero-bias current in a sliding metal––monolayer–semiconductor TENG system. Since we propose that the alkoxide anion (R–O$^-$) has an effect on the silicon band bending, given that the electrostatic force is inversely proportional to the square of the distance [73], such effect should be maximized if the length of the dielectric barrier (the carbonaceous monolayer) between semiconductor and the anion is shortened. To address this we conducted experiments analogous to those reported in the previous section (**S1**) but with a shorter monolayer, 4-pentyn-1-ol monolayer (**S2**, Scheme 1). Fig. 3 shows AFM height images and zero-bias current maps obtained on **S2** samples prepared on lowly doped n- and p-type Si(111). Negatively charged siloxyl groups from silica (oxidized Si(111)) could be a source of electrical traps and dipoles competing with the monolayer charges, but no significant signs of semiconductor oxidation, usually detectable as rounded topographical features [52,74,75], were found in the AFM height images (Fig. 3a,c). XPS data in Fig. S4 (Supporting Information) also show no evidence of oxidation. For lowly doped p-type Si(111) **S2** samples (Fig. 3d), the current signal did not raise above noise level. However, the maximum zero-bias current density on modified lowly
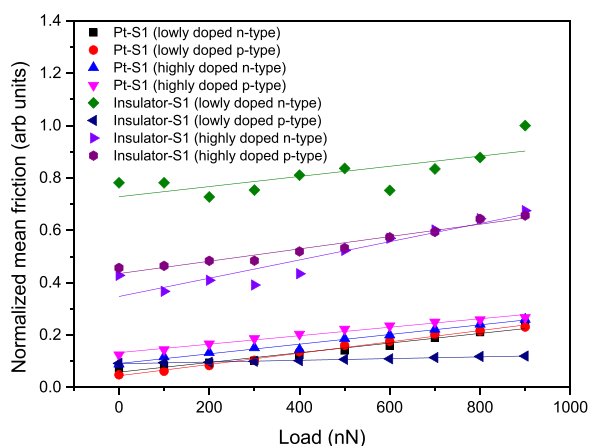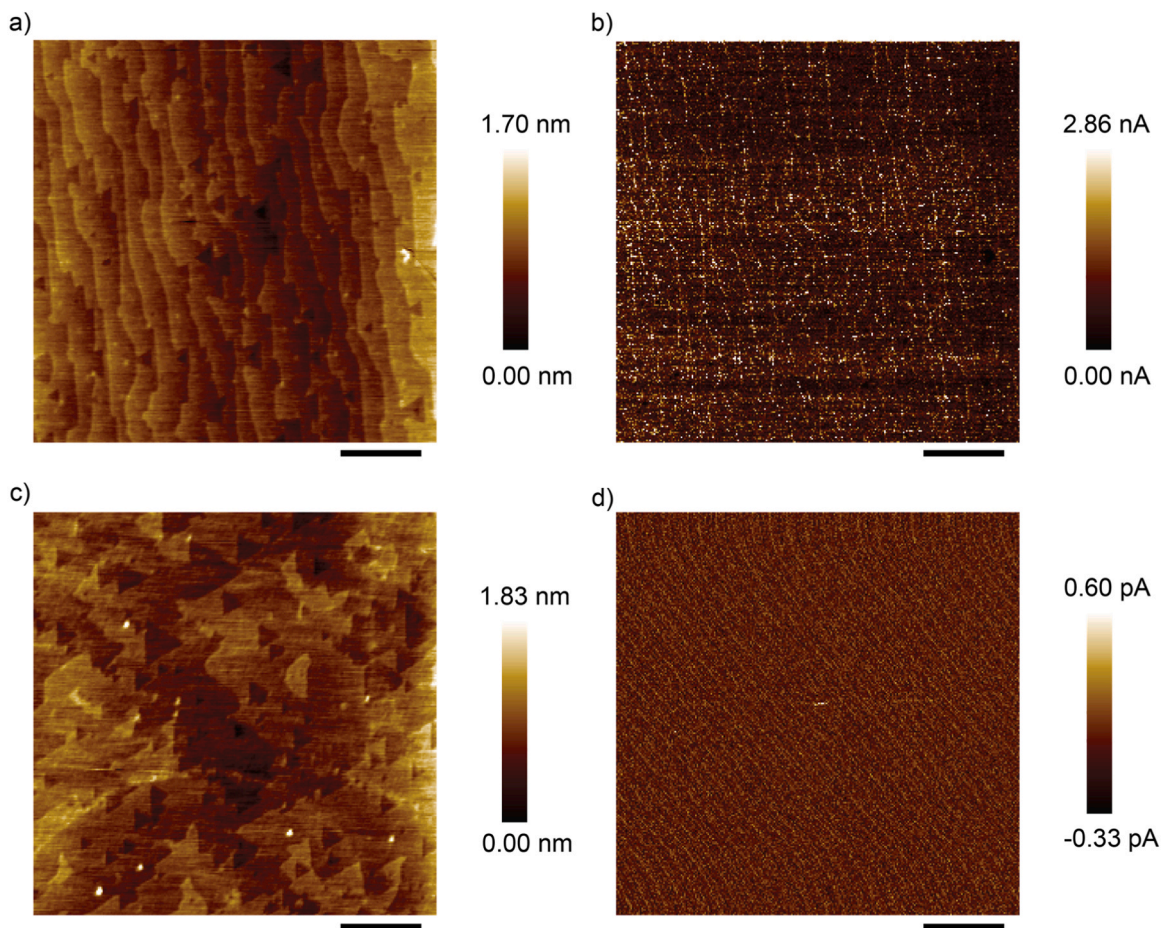

Fig. 2. Plots of the normalized mean friction (all friction data was normalized by the maximum data recorded under different loads) measured by AFM as the function of applied normal load. Samples were 8-nonyn-1-ol coated (**S1**), covalently grafted on either highly doped or lowly doped, p-type or n-type, Si(111) substrates.

Fig. 3. AFM topography images and zero-bias current maps recorded on 4-pentyn-1-ol functionalized (a-b) lowly doped n-type or (c-d) lowly doped p-type Si(111) surfaces (S2 samples). All images are obtained using platinum tip (25Pt300B). The scale bars represent 1 μm.
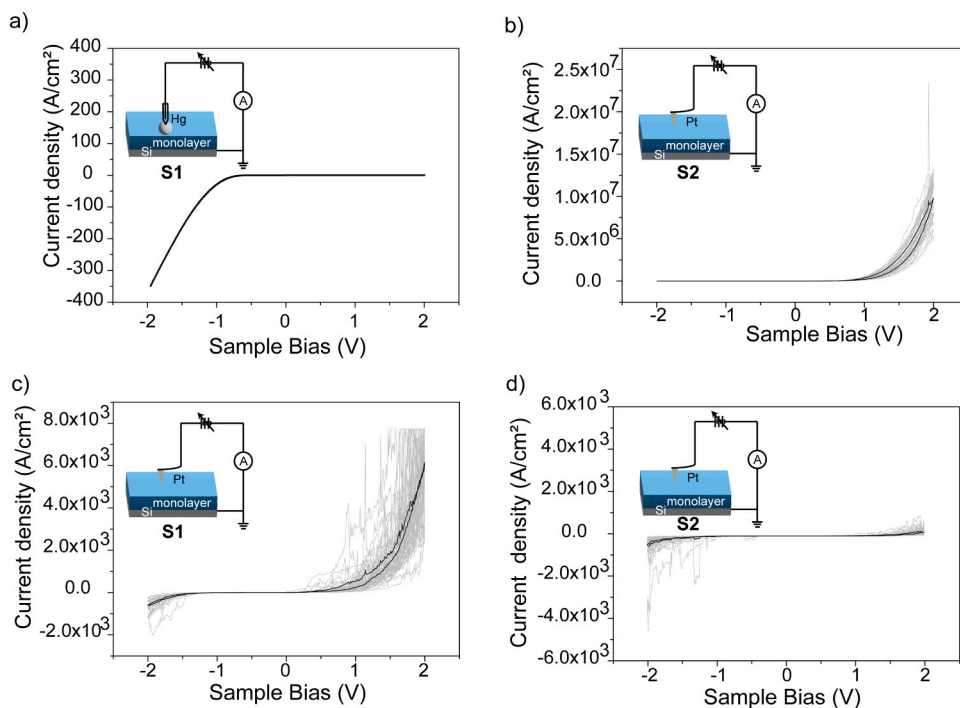
Fig. 4. (a) Current-voltage (I–V) curve obtained with a macroscopic soft contact (mercury drop, estimated pressure of ~30 Pa) on 8-nonyn-1-ol modified Si(111) surface (S1). Experimental current–voltage (I–V) spectroscopy on (b) 4-pentyn-1-ol (S2) and on (c) 8-nonyn-1-ol (S1) functionalized lowly doped n-type Si(111) surfaces, and current-voltage (I–V) spectroscopy on (d) 4-pentyn-1-ol (S2) functionalized lowly doped p-type Si(111) surfaces recorded using platinum tips (C-AFM) under an estimated contact pressure of ~5 GPa. The black thick lines in panel b–d represent the mean value of the 25 individual I–V curves plotted in gray ink. The vertical axis ranges are chosen to more clearly show the rectification characteristics of each I–V curve.

doped n-type Si(111) surface (Fig. 3b) was 3.11×10^7 A/m^2, which is comparable to the output of the longer chain samples (**S1**, 4.40×10^7 A/m^2, Fig. 1b). It appears therefore that the band bending caused by alkoxide anions (R–O–) is independent of the length of the dielectric barrier separating molecular charge and semiconductor, or that another factor dominates the zero-bias output. As investigated in the next section, one of such factors could be flexoelectricity, which is not friction-related, but pressure-related.

2.3. Flexovoltage in static junctions

According to the tabled work function difference between platinum and n-type silicon it is expected that for a "static" Schottky diode a current–voltage (I–V) curve should resemble, qualitatively, the one shown in Fig. 4a, with a reverse (blocking) bias region in the positive quadrant. For 4-pentyn-1-ol and 8-nonyn-1-ol coated surfaces (Fig. 4b,c) the difference in current density magnitude, regardless of the bias polarity, is likely to reflect the difference in the carbonaceous tunneling barrier [76,77]. More interestingly, for both surface chemistries (4-pentyn-1-ol and 8-nonyn-1-ol, **S2** and **S1**) a blocking regime typical of a diode under external reverse bias (positive semiconductor bias for n-type silicon) is happening under negative semiconductor bias, and vice-versa, a rapidly increasing current was found under positive semiconductor bias. To the best of our knowledge a similar "diode inversion" was only observed by Duan and co-workers for transferred and evaporated platinum based Schottky diodes [78], but our system is under a definitely greater junction pressure (~5 GPa), and, as such, an explanation suitable for a van der Waals diode is unlikely to be applicable here. As shown in Fig. 4a, with a soft top contact (a mercury drop) the semiconductor is under a relatively low pressure of only ~30 Pa, while in the "inverted" junctions (platinum C-AFM tip, Fig. 4b,c) the silicon is sensing around ~5 GPa. It is then important to verify whether or not such phenomenon (the inversion of the diode rectification direction) is also found on surfaces that yields no tribocurrent output. Static I–V measurements conducted on 4-pentyn-1-ol (**S2**) functionalized lowly doped p-type Si(111) surfaces (a poor TENG performer) are shown in Fig. 4d. The normal behavior of such junction would be that of allowing current to pass in the positive quadrant. This is indeed the case, but a current of similar, or even greater, magnitude is also seen in the negative quadrant. It is therefore probable that the flexovoltage has the direction of a reverse bias. Such pressure-induced voltage will therefore oppose the interfacial voltage due to static charges (friction-induced, Fig. 2), ultimately causing p-type surfaces to be poorer TENG performers (Fig. 3). In conclusion, contact pressure plays an important role that is just not causing larger friction, as the inverted I–Vs Shown in Fig. 4 were obtained when the tip is not sliding laterally. We believe that the explanation lies in the recently reported flexoelectricity under external load [79]. Under this hypothesis, external pressure would generate a flexovoltage that overwrites the instrument (external) bias, and the experimental inverted I–Vs suggest that the flexovoltage has the direction of a reverse bias. Reinforcing our interpretation of the data as the conclusions of Sun et al., who observed that current under bias could be increased by applying force on silicon based Schottky diodes [40]. Hence, we believe that the inverted diode behavior is the result of flexoelectricity under high pressure. This is evident under static conditions (Fig. 4), but it is most probably also present under dynamic (sliding) conditions. To further verify the onset of flexoelectricity we recorded the current signal while conducting F–D measurements (i.e. with no deliberate lateral movement of the junction). The result of these controls are shown in Fig. S7 (Supporting Information) and revealed a progressive increase in a positive sign current (from platinum to silicon) as the tip is forced against the silicon substrate under no external bias. Similarly to anomalous photovoltaic-to-micromechanics coupling effects in multiferroic materials [80], during the sliding process charge carriers are collected effectively by the tip and lead to a net leakage current. We believe that the DC output is the result of both tribovoltaic

and flexovoltaic effects (Fig S8, Supporting Information). The Schottky diode formed by the platinum tip and silicon surface has a built-in voltage due to differences in work functions. During the sliding process, electron–hole pairs induced by friction are separated by the junction's built-in electric field, in agreement with the output having the sign of a leakage current. In addition, there is the onset of a flexovoltage under high contact pressure. This pressure-induced (or pressure fluctuations-induced) voltage manifests as an electric field that accelerates electrons in the same direction as in response to the tribovoltage (from tip to silicon).

3. Conclusions

We have explored the connections between zero-bias current and friction, and between current and pressure in metal–monolayer–silicon Schottky diodes (dynamic and static junctions). We bring clear evidence that beside probable friction-induced electron-hole pairs, static charging of the semiconductor is a major contributor to the DC output of a sliding Schottky TENG. Friction excess is readily measurable in junctions where the current flow is prevented, it is substrate doping and type-dependent and it strongly correlates with the DC output when the current is allowed to flow under zero external bias. This excess friction is however not measurable when current flows in the TENG, and exposure of the junction to conditions that remove surface statics (UV exposure) removes the excess friction. We also show that under pressures typical of an AFM experiment there is a significant flexovoltage even when the tip is not sliding. This flexovoltage is large in systems that are good TENG performers. It can be easily detected as "inverted" diode current–voltage (I–V) characteristics, suggesting that simple and readily accessible static AFM I–V is an ideal research tool in the search and screening for optimal Schottky TENG materials. Further development of DC TENGs will benefit from an improved understanding of flexoelectricity, and materials with larger flexovoltages may represent a viable path to TENGs with a smaller reliance on friction, hence intrinsically less prone to degradation of performances under prolonged operation.

4. Material and methods

4.1. Materials

Sulfuric acid (VLSI Puranal™, 95–97 %, Honeywell), hydrogen peroxide solution (MOS Puranal™, 30 wt% in water, Honeywell), aqueous ammonium fluoride solution (40 wt%, Sigma–Aldrich), redistilled solvents and Milli-Q™ water (>18 MΩ cm) were used for silicon cleaning and etching procedures. Prime grade, single-side polished, (111)-oriented ($\pm 0.05°$) silicon wafers (Siltronix, S.A.S, Archamps, France) were 475–525 µm thick, and either lowly (7–13 Ω cm), intermediately (0.010–0.100 Ω cm) or highly doped (0.007–0.013 Ω cm), and with the exception of the wafers of intermediate doping, they were either p-type (boron-doped) or n-type (phosphorous-doped). 8-Nonyn-1-ol (97 %, Biosynth Carbosynth) and 4-pentyn-1-ol (97 %, Sigma-–Aldrich) used for monolayer assembly were used as received. Gallium–indium eutectic (99.99 %, Sigma–Aldrich) was used to ensure ohmic contact between the back of the silicon sample and the steel AFM sample holder.

4.2. Surface modification

Prior to their chemical derivatization, silicon wafers were cut into 1×1 cm squares and rinsed sequentially with dichloromethane (DCM), isopropanol, and water. Samples were then blown dry under a stream of nitrogen and immersed for 30 min in hot Piranha solution (a 3:1 mixture (v/v) of sulfuric acid (95–97 %) and hydrogen peroxide (30 %) heated to 100 °C). The clean wafers were then rinsed with water and H-terminated (Si–H) by immersion for 13 min in argon-saturated (99.997 %, Coregas) 40 % ammonium fluoride etching solution. The wafer polished side

faced upwards during the etching. The etching process was carried out under ambient light while maintaining a gentle flow of argon over the etching bath, and periodically shaking the samples so to minimize the formation of etching pits. Few grains of ammonium sulfite (~10 mg) were added to the etching solution (~20 mL of NH_4F) as oxygen scavenger. The freshly prepared Si–H samples were then rinsed with water, DCM, blown dry under a stream of nitrogen gas, and placed inside a Petri dish. The Si–H sample's polished side was then covered with 1–2 drops of either degassed 8-nonyn-1-ol or degassed 4-pentyn-1-ol. The monolayer-forming liquid was gently contacted with a 1-mm thick, 75 mm × 75 mm, quartz plate (GE 124, SPI Supplies) so to minimize liquid evaporation. The Petri dish was placed inside nitrogen-gas filled (>99.999 %, Coregas) acrylate reaction chamber. The reaction chamber was fitted with an UV light (Vilber, VL-215. M, 312 nm, nominal power output of 30 W) placed at a distance of approximately 200 mm from the samples. Samples were illuminated for 2 h while keeping the chamber under a positive pressure of nitrogen gas. The monolayer-functionalized samples (**S1** and **S2**, Scheme 1) were then rinsed with DCM, placed inside a glass reaction tube, covered with DCM, and rested at + 4 °C until analyzed.

4.3. Atomic force microscopy (AFM)

AFM topography, friction, and current maps were acquired simultaneously using the conductive AFM (C-AFM) mode of a Park NX10 (Park Systems Corporation, Suwon, Korea) fitted with a variable enhanced conductive (VECA) probe hand and FEMTO current amplifier (DLPCA-200). All AFM data were analyzed with the XEI software (Park Systems Corporation) unless specified otherwise. AFM tips were either non-conductive n-type silicon tips (TESPA-V2, Bruker, USA) with a nominal resonance frequency of 320 kHz and a spring constant of 42 N/m, or conductive solid platinum tips (25Pt300B, Rocky Mountain Nanotechnology, USA) with a nominal resonance frequency of 14 kHz and a spring constant of 18 N/m. Unless specified otherwise the scan size was set to 5 × 5 μm and the scan rate to 1.0 Hz. The current routing is such that a positive sign indicates an electronic flow from the AFM tip to the silicon sample. The reported maximum current is the 99th percentile, that is, the current at sampling points with zero-bias current output higher than 99 % of the total ~65,000 sampled points). To minimize edge artifacts, tip–sample friction data were acquired by scanning a 5 μm × 500 nm region and subtracting the retrace (scan from right to left) friction profile from the trace (scan from left to right) friction profile, and then dividing the results by 2 to obtain a friction loop image [25]. Force–distance (F–D) measurements were used to estimate adhesion force and contact area, and by setting the maximum deflection to 2000 nN, the ramp speed to 300 nm/sec, and the ramp size to 300 nm. F–D curves were processed with OriginPro 9.0 (OriginLab Corp.) to estimate the pull-off force (the force at the lowest point of the retract trace) [81]. For each sample (3 samples of each type), F–D curves were recorded at 25 separate locations over a 5 μm × 5 μm region, and the mean and standard deviation of the pull-off force, hence adhesion force, were obtained and used for contact area estimation. A titanium roughness test sample (part RS-12 M, Bruker, USA) was used to estimate the tip radius by analyzing the experimental topography data in Gwyddion 2.59 (Czech Metrology Institute) through the blind estimation software function. The silicon–platinum contact area of each sample was estimated against the Derjaguin, Muller and Toporov (DMT) model of adhesion [36,82,83] covered in Section S1 of the Supporting Information. For all current-potential (I–V) measurements, a 360 nN set point was selected. The external bias was ramped between − 2.0 and 2.0 V at a sweep rate of 8 V/s. I–Vs were sampled at 25 evenly distributed sample locations across a 5 × 5 μm sample area. Platinum tips (25Pt300B) were used for the I–V measurements. Before each measurement the open-circuit current was manually adjusted to zero.

4.4. Macroscopic current-voltage (I–V) measurements with soft metal contacts

Current–voltage (I–V) measurements of silicon–monolayer–mercury junctions were conducted inside a lightproof and grounded Faraday cage, with a source–measure unit (model B2902A, Keysight) and a spherical mercury top contact controlled by a hanging electrode apparatus (HMDE WK2, Institute of Physical Chemistry, Polish Academy of Sciences). The voltage was ramped cyclically between − 2.0 and 2.0 V in steps of 20 mV. The duration of each step was of 400 ms, and the current signal was sampled after a 300 ms delay from the potential step-up event. The bias routing is from the semiconductor to the metal, so to match the AFM settings, and two voltage ramps were recorded for each sampling location on individually prepared and analyzed samples. A minimum of three sampling locations on each sample were analyzed. Current values were corrected by the contact area of the metal–semiconductor junction. The contact area was estimated from brightfield optical images acquired with a CCD camera (DCC1240C, Thorlabs) fitted with a 6.5 × zoom (MVL6×123Z and MVL133A, Thorlabs). Silicon samples were scribed with emery paper before and after applying a small amount of gallium−indium eutectic to ensure the ohmic contact between the back of the silicon sample and a copper plate. All images were analyzed using Fiji image processing software [84], and data were analyzed and plotted using OriginPro 9.0 (OriginLab Corp.).

4.5. X-ray photoelectron spectroscopy (XPS)

XPS analysis of the silicon surfaces was performed on a Kratos Axis Ultra DLD (Kratos Analytical Ltd, UK) fitted with a monochromatic Al Kα (1486.6 eV) radiation source operating at 225 W, and a hemispherical analyzer (165 mm radius) running in fixed analyzer transmission mode. The photoelectron take-off angle was normal to the sample, and the chamber operated at 2×10^{-8} Torr. The analysis area was 300 × 700 μm, and an internal flood gun was used to minimize sample charging. Survey spectra (accumulation of three scans) were acquired between 0 and 1100 eV, with a dwell time of 55 ms, a pass energy of 160 eV, and a step size of 0.5 eV. High-resolution scans (accumulation of 10 scans) used a pass energy of 20 eV, and a step size of either 0.05 eV (Si 2p, 95–110 eV), or 0.1 eV (C 1 s, 274–298 eV) [51,85–89]. XPS data were processed in CasaXPS (version 2.3.18) and any residual charging was corrected by applying a rigid shift to bring the main C 1 s emission (C–C) to 285.0 eV.

CRediT authorship contribution statement

Xin Lyu: Investigation, Methodology, Software, Formal analysis, Visualization, Writing – original draft, Writing – review & editing. **Melanie MacGregor:** Investigation, Formal analysis, Funding acquisition, Writing – review & editing. **Jun Liu:** Methodology, Validation, Writing – review & editing. **Nadim Darwish:** Investigation, Formal analysis, Funding acquisition, Writing – review & editing. **Simone Ciampi:** Conceptualization, Methodology, Supervision, Validation, Data curation, Project administration, Writing – review & editing, Formal analysis, Funding acquisition.

Declaration of Competing Interest

The authors declare that they have no known competing financial interests or personal relationships that could have appeared to influence the work reported in this paper.

Data availability

Data will be made available on request.

Acknowledgements

Appendix A. Supporting information

Supplementary data associated with this article can be found in the online version at doi:10.1016/j.nanoen.2023.108627.

References

[1] Kahn, F.J., The digital revolution in electronic projection display technology, SID International Symposium Digest of Technical Papers 31 (2000) 302–305. http://doi.org/10.1889/1.1832943.

[2] F.G. Reamer, The digital and electronic revolution in social work: rethinking the meaning of ethical practice, Ethics Soc. Welf. 7 (2013) 2–19, https://doi.org/10.1080/17496535.2012.738694.

[3] S. Niu, Z.L. Wang, Theoretical systems of triboelectric nanogenerators, Nano Energy 14 (2015) 161–192, https://doi.org/10.1016/j.nanoen.2014.11.034.

[4] Y.C. Lai, J. Deng, S.L. Zhang, S. Niu, H. Guo, Z.L. Wang, Single-thread-based wearable and highly stretchable triboelectric nanogenerators and their applications in cloth-based self-powered human-interactive and biomedical sensing, Adv. Funct. Mater. 27 (2017), 1604462, https://doi.org/10.1002/adfm.201604462.

[5] Z. Lin, J. Yang, X. Li, Y. Wu, W. Wei, J. Liu, J. Chen, J. Yang, Large-scale and washable smart textiles based on triboelectric nanogenerator arrays for self-powered sleeping monitoring, Adv. Funct. Mater. 28 (2018), 1704112, https://doi.org/10.1002/adfm.201704112.

[6] X. Wang, J. Song, J. Liu, L.W. Zhong, Direct-current nanogenerator driven by ultrasonic waves, Science 316 (2007) 102–105, https://doi.org/10.1126/science.1139366.

[7] M. Salauddin, R.M. Toyabur, P. Maharjan, M.S. Rasel, J.W. Kim, H. Cho, J.Y. Park, Miniaturized springless hybrid nanogenerator for powering portable and wearable electronic devices from human-body-induced vibration, Nano Energy 51 (2018) 61–72, https://doi.org/10.1016/j.nanoen.2018.06.042.

[8] Y. Liang, C.Z. Zhao, H. Yuan, Y. Chen, W. Zhang, J.Q. Huang, D. Yu, Y. Liu, M. M. Titirici, Y.L. Chueh, H. Yu, Q. Zhang, A review of rechargeable batteries for portable electronic devices, InfoMat 1 (2019) 6–32, https://doi.org/10.1002/inf2.12000.

[9] C. Wu, A.C. Wang, W. Ding, H. Guo, Z.L. Wang, Triboelectric nanogenerator: a foundation of the energy for the new era, Adv. Energy Mater. 9 (2019), 1802906, https://doi.org/10.1002/aenm.201802906.

[10] Z.L.A. Wang. Triboelectric Nanogenerators, first ed., Springer International Publishing: Imprint: Springer,, Cham, 2016.

[11] Z.L. Wang, Triboelectric nanogenerators as new energy technology for self-powered systems and as active mechanical and chemical sensors, ACS Nano 7 (2013) 9533–9557, https://doi.org/10.1021/nn404614z.

[12] Y. Zi, H. Guo, Z. Wen, M.-H. Yeh, C. Hu, Z.L. Wang, Harvesting low-frequency (<5 Hz) irregular mechanical energy: a possible killer application of triboelectric nanogenerator, ACS Nano 10 (2016) 4797–4805, https://doi.org/10.1021/acsnano.6b01569.

[13] M.-L. Seol, J.-H. Woo, S.-B. Jeon, D. Kim, S.-J. Park, J. Hur, Y.-K. Choi, Vertically stacked thin triboelectric nanogenerator for wind energy harvesting, Nano Energy 14 (2015) 201–208, https://doi.org/10.1016/j.nanoen.2014.11.016.

[14] J.H. Lee, S. Kim, T.Y. Kim, U. Khan, S.-W. Kim, Water droplet-driven triboelectric nanogenerator with superhydrophobic surfaces, Nano Energy 58 (2019) 579–584, https://doi.org/10.1016/j.nanoen.2019.01.078.

[15] S. Lin, X. Chen, Z.L. Wang, The tribovoltaic effect and electron transfer at a liquid-semiconductor interface, Nano Energy 76 (2020), 105070, https://doi.org/10.1016/j.nanoen.2020.105070.

[16] L. Liu, Z. Zhao, Y. Li, X. Li, D. Liu, S. Li, Y. Gao, L. Zhou, J. Wang, Z.L. Wang, Achieving ultrahigh effective surface charge density of direct-current triboelectric nanogenerator in high humidity, Small (2022), e2201402, https://doi.org/10.1002/smll.202201402.

[17] R. Xu, Q. Zhang, J.Y. Wang, D. Liu, J. Wang, Z.L. Wang, Direct current triboelectric cell by sliding an n-type semiconductor on a p-type semiconductor, Nano Energy 66 (2019), 104185, https://doi.org/10.1016/j.nanoen.2019.104185.

[18] J. Liu, A. Goswami, K.R. Jiang, F. Khan, S. Kim, R. McGee, Z. Li, Z.Y. Hu, J. Lee, T. Thundat, Direct-current triboelectricity generation by a sliding Schottky nanocontact on MoS$_2$ multilayers. Nat. Nanotechnol. 13 (2018) 112–116, https://doi.org/10.1038/s41565-017-0019-5.

[19] S. Lin, Y. Lu, S. Feng, Z. Hao, Y. Yan, A high current density direct-current generator based on a moving van der Waals Schottky diode, Adv. Mater. 31 (2018), 1804398, https://doi.org/10.1002/adma.201804398.

[20] Z. You, S. Wang, Z. Li, Y. Zou, T. Lu, F. Wang, B. Hu, X. Wang, L. Li, W. Fang, Y. Liu, High current output direct-current triboelectric nanogenerator based on organic semiconductor heterojunction, Nano Energy 91 (2022), 106667, https://doi.org/10.1016/j.nanoen.2021.106667.

[21] R. Yang, M. Benner, Z. Guo, C. Zhou, J. Liu, High-performance flexible Schottky DC generator via metal/conducting polymer sliding contacts, Adv. Funct. Mater. 31 (2021), 2103132, https://doi.org/10.1002/adfm.202103132.

[22] S. Chen, D. Liu, L. Zhou, S. Li, Z. Zhao, S. Cui, Y. Gao, Y. Li, Z.L. Wang, J. Wang, Improved output performance of direct-current triboelectric nanogenerator through field enhancing breakdown effect, Adv. Mater. Technol. 6 (2021), 2100195, https://doi.org/10.1002/admt.202100195.

[23] Y. Lu, Q. Gao, X. Yu, H. Zheng, R. Shen, Z. Hao, Y. Yan, P. Zhang, Y. Wen, G. Yang, S. Lin, Interfacial built-in electric field-driven direct current generator based on dynamic silicon homojunction, Research 2020 (2020), 5714754, https://doi.org/10.34133/2020/5714754.

[24] X. Huang, X. Xiang, J. Nie, D. Peng, F. Yang, Z. Wu, H. Jiang, Z. Xu, Q. Zheng, Microscale Schottky superlubric generator with high direct-current density and ultralong life, Nat. Commun. 12 (2021) 2268, https://doi.org/10.1038/s41467-021-22371-1.

[25] S. Ferrie, A.P. Le Brun, G. Krishnan, G.G. Andersson, N. Darwish, S. Ciampi, Sliding silicon-based Schottky diodes: maximizing triboelectricity with surface chemistry, Nano Energy 93 (2022), 106861, https://doi.org/10.1016/j.nanoen.2021.106861.

[26] S. Ferrie, N. Darwish, J.J. Gooding, S. Ciampi, Harnessing silicon facet-dependent conductivity to enhance the direct-current produced by a sliding Schottky diode triboelectric nanogenerator, Nano Energy 78 (2020), 105210, https://doi.org/10.1016/j.nanoen.2020.105210.

[27] X. Lyu, S. Ferrie, A. Pivrikas, M. MacGregor, S. Ciampi, Sliding Schottky diode triboelectric nanogenerators with current output of 10^9A/m^2 by molecular engineering of Si(211) surfaces. Nano Energy (2022), 107658 https://doi.org/10.1016/j.nanoen.2022.107658.

[28] C. Xu, J. Yu, Z. Huo, Y. Wang, Q. Sun, Z.L. Wang, Pursuing the tribovoltaic effect for direct-current triboelectric nanogenerators, Energy Environ. Sci. 16 (2023) 983–1006, https://doi.org/10.1039/d2ee04019k.

[29] R. Yang, R. Xu, W. Dou, M. Benner, Q. Zhang, J. Liu, Semiconductor-based dynamic heterojunctions as an emerging strategy for high direct-current mechanical energy harvesting, Nano Energy 83 (2021), 105849, https://doi.org/10.1016/j.nanoen.2021.105849.

[30] X. Lyu, S. Ciampi, Improving the performances of direct-current triboelectric nanogenerators with surface chemistry, Curr. Opin. Colloid Interface Sci. 61 (2022), https://doi.org/10.1016/j.cocis.2022.101627.

[31] V.A. Sharov, P.A. Alekseev, B.R. Borodin, M.S. Dunaevskiy, R.R. Reznik, G. E. Cirlin, InP/Si heterostructure for high-current hybrid triboelectric/photovoltaic generation, ACS Appl. Energy Mater. 2 (2019) 4395–4401, https://doi.org/10.1021/acsaem.9b00576.

[32] C. Hurtado, X. Lyu, S. Ferrie, A.P. Le Brun, M. MacGregor, S. Ciampi, Organic monolayers on Si(211) for triboelectricity generation: etching optimization and relationship between the electrochemistry and current output, ACS Appl. Nano Mater. 5 (2022) 14263–14274, https://doi.org/10.1021/acsanm.2c02006.

[33] J. Xu, Y. Zou, A. Nashalian, J. Chen, Leverage surface chemistry for high-performance triboelectric nanogenerators, Front. Chem. 8 (2020), 577327, https://doi.org/10.3389/fchem.2020.577327.

[34] S. Wang, Y. Zi, Y.S. Zhou, S. Li, F. Fan, L. Lin, Z.L. Wang, Molecular surface functionalization to enhance the power output of triboelectric nanogenerators, J. Mater. Chem. A 4 (2016) 3728–3734, https://doi.org/10.1039/c5ta10239a.

[35] S. Pan, N. Yin, Z. Zhang, Time- & Load-dependence of triboelectric effect, Sci. Rep. 8 (2018) 2470, https://doi.org/10.1038/s41598-018-20937-6.

[36] J.Y. Park, M. Salmeron, Fundamental aspects of energy dissipation in friction, Chem. Rev. 114 (2014) 677–711, https://doi.org/10.1021/cr200431y.

[37] J.Y. Park, D.F. Ogletree, P.A. Thiel, M. Salmeron, Electronic control of friction in silicon pn junctions, Science 313 (2006) 186, https://doi.org/10.1126/science.1125017.

[38] Z. Zhang, D. Jiang, J. Zhao, G. Liu, T. Bu, C. Zhang, Z.L. Wang, Tribovoltaic effect on metal–semiconductor interface for direct-current low-impedance triboelectric nanogenerators, Adv. Energy Mater. 10 (2020), 1903713, https://doi.org/10.1002/aenm.201903713.

[39] C.A. Mizzi, L.D. Marks, When flexoelectricity drives triboelectricity, Nano Lett. 22 (2022) 3939–3945, https://doi.org/10.1021/acs.nanolett.2c00240.

[40] L. Sun, L. Zhu, C. Zhang, W. Chen, Z. Wang, Mechanical manipulation of silicon-based Schottky diodes via flexoelectricity, Nano Energy 83 (2021), 105855, https://doi.org/10.1016/j.nanoen.2021.105855.

[41] J. Liu, K. Jiang, L. Nguyen, Z. Li, T. Thundat, Interfacial friction-induced electronic excitation mechanism for tribo-tunneling current generation, Mater. Horiz. 6 (2019) 1020–1026, https://doi.org/10.1039/c8mh01259h.

[42] Y.B. Qi, J.Y. Park, B.L.M. Hendriksen, D.F. Ogletree, M. Salmeron, Electronic contribution to friction on GaAs: an atomic force microscope study, Phys. Rev. B 77 (2008), https://doi.org/10.1103/PhysRevB.77.184105.

[43] P. Chen, J. An, S. Shu, R. Cheng, J. Nie, T. Jiang, Z.L. Wang, Super-durable, low-wear, and high-performance fur-brush triboelectric nanogenerator for wind and water energy harvesting for smart agriculture, Adv. Energy Mater. 11 (2021), 2003066, https://doi.org/10.1002/aenm.202003066.

[44] H.A. Spikes, Triboelectrochemistry: influence of applied electrical potentials on friction and wear of lubricated contacts, Tribol. Lett. 68 (2020), https://doi.org/10.1007/s11249-020-01328-3.

[45] J. Liu, M. Miao, K. Jiang, F. Khan, A. Goswami, R. McGee, Z. Li, L. Nguyen, Z. Hu, J. Lee, K. Cadien, T. Thundat, Sustained electron tunneling at unbiased metal-insulator-semiconductor triboelectric contacts, Nano Energy 48 (2018) 320–326, https://doi.org/10.1016/j.nanoen.2018.03.068.

[46] Y. Dong, Effects of substrate roughness and electron–phonon coupling on thickness-dependent friction of graphene, J. Phys. D Appl. Phys. 47 (2014), 055305, https://doi.org/10.1088/0022-3727/47/5/055305.

[47] J.Y. Park, Y. Qi, D.F. Ogletree, P.A. Thiel, M. Salmeron, Influence of carrier density on the friction properties of siliconpnjunctions, Phys. Rev. B Condens. Matter Mater. Phys. 76 (2007), https://doi.org/10.1103/PhysRevB.76.064108.

[48] M.R. Linford, C.E.D. Chidsey, Alkyl monolayers covalently bonded to silicon surfaces, J. Am. Chem. Soc. 115 (1993) 12631–12632, https://doi.org/10.1021/ja00079a071.

[49] M.R. Linford, P. Fenter, P.M. Eisenberger, C.E.D. Chidsey, Alkyl monolayers on silicon prepared from 1-alkenes and hydrogen-terminated silicon, J. Am. Chem. Soc. 117 (1995) 3145–3155, https://doi.org/10.1021/ja00116a019.

[50] S. Zhang, S. Ferrie, X. Lyu, Y. Xia, N. Darwish, Z. Wang, S. Ciampi, Absence of a relationship between surface conductivity and electrochemical rates: redox-active monolayers on Si(211), Si(111), and Si(110), J. Phys. Chem. C 125 (2021) 18197–18203, https://doi.org/10.1021/acs.jpcc.1c05023.

[51] S. Zhang, S. Ferrie, C.R. Peiris, X. Lyu, Y.B. Vogel, N. Darwish, S. Ciampi, Common background signals in voltammograms of crystalline silicon electrodes are reversible silica–silicon redox chemistry at highly conductive surface sites, J. Am. Chem. Soc. 143 (2021) 1267–1272, https://doi.org/10.1021/jacs.0c10713.

[52] Y.B. Vogel, L. Zhang, N. Darwish, V.R. Gonçales, A. Le Brun, J.J. Gooding, A. Molina, G.G. Wallace, M.L. Coote, J. Gonzalez, S. Ciampi, Reproducible flaws unveil electrostatic aspects of semiconductor electrochemistry, Nat. Commun. 8 (2017) 2066, https://doi.org/10.1038/s41467-017-02091-1.

[53] L. Zhang, E. Laborda, N. Darwish, B.B. Noble, J.H. Tyrell, S. Pluczyk, A.P. Le Brun, G.G. Wallace, J. Gonzalez, M.L. Coote, S. Ciampi, Electrochemical and electrostatic cleavage of alkoxyamines, J. Am. Chem. Soc. 140 (2018) 766–774, https://doi.org/10.1021/jacs.7b11628.

[54] L. Zhang, Y.B. Vogel, B.B. Noble, V.R. Gonçales, N. Darwish, A.L. Brun, J. J. Gooding, G.G. Wallace, M.L. Coote, S. Ciampi, TEMPO monolayers on Si(100) electrodes: electrostatic effects by the electrolyte and semiconductor space-charge on the electroactivity of a persistent radical, J. Am. Chem. Soc. 138 (2016) 9611–9619, https://doi.org/10.1021/jacs.6b04788.

[55] S. Li, J. Nie, Y. Shi, X. Tao, F. Wang, J. Tian, S. Lin, X. Chen, Z.L. Wang, Contributions of different functional groups to contact electrification of polymers, Adv. Mater. 32 (2020), e2001307, https://doi.org/10.1002/adma.202001307.

[56] S.-H. Shin, Y.H. Kwon, Y.-H. Kim, J.-Y. Jung, M.H. Lee, J. Nah, Triboelectric charging sequence induced by surface functionalization as a method to fabricate high performance triboelectric generators, ACS Nano 9 (2015) 4621–4627, https://doi.org/10.1021/acsnano.5b01340.

[57] A. Ahmed, I. Hassan, A.M. Pourrahimi, A.S. Helal, M.F. El-Kady, H. Khassaf, R. B. Kaner, Toward high-performance triboelectric nanogenerators by engineering interfaces at the nanoscale: looking into the future research roadmap, Adv. Mater. Technol. 5 (2020), 2000520, https://doi.org/10.1002/admt.202000520.

[58] M. Zheng, S. Lin, Z. Tang, Y. Feng, Z.L. Wang, Photovoltaic effect and tribovoltaic effect at liquid-semiconductor interface, Nano Energy 83 (2021), 105810, https://doi.org/10.1016/j.nanoen.2021.105810.

[59] M. Zheng, S. Lin, L. Xu, L. Zhu, Z.L. Wang, Scanning probing of the tribovoltaic effect at the sliding interface of two semiconductors, Adv. Mater. 32 (2020), e2000928, https://doi.org/10.1002/adma.202000928.

[60] Z. Zhang, Z. Wang, Y. Chen, Y. Feng, S. Dong, H. Zhou, Z.L. Wang, C. Zhang, Semiconductor contact-electrification-dominated tribovoltaic effect for ultrahigh power generation, Adv. Mater. 34 (2022), e2200146, https://doi.org/10.1002/adma.202200146.

[61] X. Xu, J. Li, X. Tao, Q. Yan, H. Wu, Z. Guan, L. Liu, X. Chen, W. Ou-Yang, Study of interfacial design for direct-current tribovoltaic generators, Nano Energy 94 (2022), 106957, https://doi.org/10.1016/j.nanoen.2022.106957.

[62] D. Yang, L. Zhang, N. Luo, Y. Liu, W. Sun, J. Peng, M. Feng, Y. Feng, H. Wang, D. Wang, Tribological-behaviour-controlled direct-current triboelectric nanogenerator based on the tribovoltaic effect under high contact pressure, Nano Energy 99 (2022), 107370, https://doi.org/10.1016/j.nanoen.2022.107370.

[63] W. Wang, A. Yu, X. Liu, Y. Liu, Y. Zhang, Y. Zhu, Y. Lei, M. Jia, J. Zhai, Z.L. Wang, Large-scale fabrication of robust textile triboelectric nanogenerators, Nano Energy 71 (2020), 104605, https://doi.org/10.1016/j.nanoen.2020.104605.

[64] L. Lin, Y. Xie, S. Niu, S. Wang, P.-K. Yang, Z.L. Wang, Robust triboelectric nanogenerator based on rolling electrification and electrostatic induction at an instantaneous energy conversion efficiency of ~55. ACS Nano 9 (2015) 922–930, https://doi.org/10.1021/nn506673x.

[65] H. Zou, L. Guo, H. Xue, Y. Zhang, X. Shen, X. Liu, P. Wang, X. He, G. Dai, P. Jiang, H. Zheng, B. Zhang, C. Xu, Z.L. Wang, Quantifying and understanding the triboelectric series of inorganic non-metallic materials, Nat. Commun. 11 (2020) 2093, https://doi.org/10.1038/s41467-020-15926-1.

[66] H. Inaba, T. Ohmi, T. Yoshida, T. Okada, Neutralization of static electricity by soft X-rays and vacuum UV radiation, J. Electrost. 33 (1994) 15–42, https://doi.org/10.1016/0304-3886(94)90061-2.

[67] Y. Gosho, M. Yamada, M. Saeki, Static charge elimination of charged matter using UV lamp, Jpn. J. Appl. Phys., Part 1 29 (1990) 950–951, https://doi.org/10.1143/JJAP.29.950.

[68] X.G. Zhang, Electrochemistry of Silicon and Its Oxide, Springer, US: Boston, MA, 2001, https://doi.org/10.1007/b100331.

[69] I. Burgess, B. Seivewright, R.B. Lennox, Electric field driven protonation/deprotonation of self-assembled monolayers of acid-terminated thiols, Langmuir 22 (2006) 4420–4428, https://doi.org/10.1021/la052767g.

[70] P. Kolodner, E.P. Lukashev, Y.-C. Ching, D.L. Rousseau, Electric-field-induced Schiff-base deprotonation in D85N mutant bacteriorhodopsin, Proc. Natl. Acad. Sci. USA 93 (1996) 11618–11621, https://doi.org/10.1073/pnas.93.21.11618.

[71] M.F. Delley, E.M. Nichols, J.M. Mayer, Interfacial acid–base equilibria and electric fields concurrently probed by in situ surface-enhanced infrared spectroscopy, J. Am. Chem. Soc. 143 (2021) 10778–10792, https://doi.org/10.1021/jacs.1c05419.

[72] K.P. Olson, C.A. Mizzi, L.D. Marks, Band bending and ratcheting explain triboelectricity in a flexoelectric contact diode, Nano Lett. 22 (2022) 3914–3921, https://doi.org/10.1021/acs.nanolett.2c00107.

[73] D. Halliday, R. Resnick, J. Walker. Fundamentals of Physics, seventh, extended ed., Wiley, Hoboken, NJ, 2005.

[74] T. Li, E.M. Dief, X. Lyu, S. Rahpeima, S. Ciampi, N. Darwish, Nanoscale silicon oxide reduces electron transfer kinetics of surface-bound ferrocene monolayers on dilicon, J. Phys. Chem. C 125 (2021) 27763–27770, https://doi.org/10.1021/acs.jpcc.1c07788.

[75] M. Filipescu, Functional Metal Oxide Thin Films Grown by Pulsed Laser Deposition, IntechOpen, 2016, https://doi.org/10.5772/62986.

[76] O. Yaffe, L. Scheres, L. Segev, A. Biller, I. Ron, E. Salomon, M. Giesbers, A. Kahn, L. Kronik, H. Zuilhof, A. Vilan, D. Cahen, Hg/molecular monolayer−Si junctions: electrical interplay between monolayer properties and semiconductor doping density, J. Phys. Chem. C 114 (2010) 10270–10279, https://doi.org/10.1021/jp101656t.

[77] E.J. Faber, L.C.P.M. de Smet, W. Olthuis, H. Zuilhof, E.J.R. Sudhölter, P. Bergveld, A. van den Berg, Si-C linked organic monolayers on crystalline silicon surfaces as alternative gate insulators, ChemPhysChem 6 (2005) 2153–2166, https://doi.org/10.1002/cphc.200500120.

[78] Y. Liu, J. Guo, E. Zhu, L. Liao, S.-J. Lee, M. Ding, I. Shakir, V. Gambin, Y. Huang, X. Duan, Approaching the Schottky-Mott limit in van der Waals metal-semiconductor junctions, Nature 557 (2018) 696–700, https://doi.org/10.1038/s41586-018-0129-8.

[79] C.A. Mizzi, A.Y.W. Lin, L.D. Marks, Does flexoelectricity drive triboelectricity? Phys. Rev. Lett. 123 (2019) 1, https://doi.org/10.1103/PhysRevLett.123.116103.

[80] M. Alexe, D. Hesse, Tip-enhanced photovoltaic effects in bismuth ferrite, Nat. Commun. 2 (2011) 256, https://doi.org/10.1038/ncomms1261.

[81] Y.F. Dufrêne, D. Martínez-Martín, I. Medalsy, D. Alsteens, D.J. Müller, Multiparametric imaging of biological systems by force-distance curve-based AFM, Nat. Methods 10 (2013) 847–854, https://doi.org/10.1038/nmeth.2602.

[82] J.Y. Park, M. Salmeron, Fundamental aspects of energy dissipation in friction, Chem. Rev. 114 (2014) 677–711, https://doi.org/10.1021/cr200431y.

[83] S.K. Hassel Ledbetter, Monocrystal elastic constants and derived properties of the cubic and the hexagonal elements, in: M. Levy, H.E. B., R.R. Stern, L. Furr, V. Keppens (Eds.), Handbook of Elastic Properties of Solids, Liquids and Gases, Academic Press, San Diego, 2001, pp. 97–106.

[84] J. Schindelin, I. Arganda-Carreras, E. Frise, V. Kaynig, M. Longair, T. Pietzsch, S. Preibisch, C. Rueden, S. Saalfeld, B. Schmid, J.-Y. Tinevez, D.J. White, V. Hartenstein, K. Eliceiri, P. Tomancak, A. Cardona, Fiji: an open-source platform for biological-image analysis, Nat. Methods 9 (2012) 676–682, https://doi.org/10.1038/nmeth.2019.

[85] G.F. Cerofolini, C. Galati, L. Renna, Accounting for anomalous oxidation states of silicon at the Si/SiO₂ interface. Surf. Interface Anal. 33 (2002) 583–590, https://doi.org/10.1002/sia.1424.

[86] J.E. Baio, T. Weidner, J. Brison, D.J. Graham, L.J. Gamble, D.G. Castner, Amine terminated SAMs: investigating why oxygen is present in these films, J. Electron Spectrosc. Relat. Phenom. 172 (2009) 2–8, https://doi.org/10.1016/j.elspec.2009.02.008.

[87] O. Yaffe, L. Scheres, L. Segev, A. Biller, I. Ron, E. Salomon, M. Giesbers, A. Kahn, L. Kronik, H. Zuilhof, A. Vilan, D. Cahen, Hg/Molecular monolayer−Si junctions: electrical interplay between monolayer properties and semiconductor doping density, J. Phys. Chem. C 114 (2010) 10270–10279, https://doi.org/10.1021/jp101656t.

[88] L. Scheres, A. Arafat, H. Zuilhof, Self-assembly of high-quality covalently bound organic monolayers onto silicon, Langmuir 23 (2007) 8343–8346, https://doi.org/10.1021/la701359k.

[89] X. Wallart, C. Henry de Villeneuve, P. Allongue, Truly quantitative XPS characterization of organic monolayers on silicon: study of alkyl and alkoxy monolayers on H−Si(111), J. Am. Chem. Soc. 127 (2005) 7871–7878, https://doi.org/10.1021/ja0430797.